Modelling the motion of organelles in an elongated cell via the coordination of heterogeneous drift-diffusion and long-range transport

Congping Lin[1,2,3], Peter Ashwin[4], Gero Steinberg[5]

[1]School of Mathematics and Statistics, [2]Center for Mathematical Sciences,

[3]Hubei Key Lab of Engineering Modeling and Scientific Computing

Huazhong University of Science and Technology, Wuhan, China

[4]Mathematics Research Institute and [5] School of Biosciences, University of Exeter, Exeter UK

(December 1, 2020)

Abstract

Cellular distribution of organelles in living cells is achieved via a variety of transport mechanisms, including directed motion, mediated by molecular motors along microtubules (MTs), and diffusion which is predominantly heterogeneous in space. In this paper, we introduce a model for particle transport in elongated cells that couples poleward drift, long-range bidirectional transport and diffusion with spatial heterogeneity in a three dimensional space. Using stochastic simulations and analysis of a related population model, we find parameter regions where the three-dimensional model can be reduced to a coupled one-dimensional model or even a one-dimensional scalar model. We explore the efficiency with which individual model components can overcome drift towards one of the cell poles to reach approximately even distributions. In particular, we find that when lateral movement is well mixed, increasing binding ability of particles to MTs is an efficient way to overcome a poleward drift. When lateral motion is not well mixed, increasing the axial diffusivity away from MTs becomes an efficient way to overcome the poleward drift. Our three-dimensional model provides a new tool that will help to understand the mechanisms by which eukaryotic cells organise their organelles in an elongated cell, and in particular when the one-dimensional models are applicable.

Key words: intracellular transport, transport coordination, skew diffusion, drift-diffusion

1 Introduction

1.1 Coordinated transport processes within the living cell

Physiology and survival of eukaryotic cells depends on proper spatial organization of vesicles or organelles. For instance, organelles that are involved in lipid homeostasis and fatty acid metabolism, such as peroxisomes and lipid droplets, are evenly positioned. This may foster dynamic interaction to transfer and distribute lipids, exchange metabolites or transduce signals [1] and is thought to be of critical importance to their functional role in reactive oxygen species homeostasis [2]. A random distribution of organelles can be achieved by various types of intracellular transport including diffusion and directed motion. In living cells, both diffusion and directed motion are important for organelle/vesicle transport and stochastic transitions between them has also been reported for several organelles [2, 3, 4, 5].

Long-range directed transport is mediated by molecular motors such as plus end-directed kinesins and minus end-directed dyneins, which use the polarity of microtubules (MTs) in the cell for bidirectional organelle motility [6]. In contrast, diffusion of particles is generally assumed to underpin in random organelle motility (see [2] and references therein). In addition short range motility of organelles occurs in living cells [7, 8] which might be driven by unidirectional motion associated with cytoplasmic flow [9]. Coordination between diffusive transport and directed transport has been studied in various systems [10, 11, 12]. In particular, within the fungus *Ustilago maydis* where the cytoskeletal architecture and molecular basis of motor motility and membrane trafficking is well understood [13, 14]. In this system it was shown that active diffusion and directed transport cooperate to distribute organelles against a poleward drift, mediated by actin-based processes [2].

Diffusive behaviors within the cytoplasm can be complicated and highly heterogeneous. Enhancement of passive diffusion by ATP-dependent movements in the cell (also known as "active diffusion") as well as anomalous diffusion behaviour (subdiffusion or superdiffusion) has been observed in living cells [15, 16, 17, 18, 19, 20, 21]. Enhanced diffusion could be due to motor-based stirring of the cytoplasm, movement on a random network within the cytoskeleton, or transient interactions with moving motors/cargos [15, 16, 22, 23, 24]. Anomalous diffusion can be associated with transient immobilization or trapping, molecular crowding or cytoskeletal networks that impose obstacles around diffusing molecules [25]. As a consequence, diffusion process inside cells could be inhomogeneous and space dependent. In particular, studies on membrane trafficking in

the elongated hyphal cells of the model fungus *U. maydis* have shown that MT-based bidirectional motility of organelles (in particular early endosomes), as well as cytoplasmic particles (e.g. ribosomes) interacting with early endosomes, enhance the diffusion of peroxisomes near MTs, by potential collisions [26, 2]. This adds to the growing body of evidence that organelles and vesicles undergo diffusion with heterogeneity.

1.2 Modelling coordinated transport

Mathematical modelling has already elucidated many basic aspects of cargo transport and motor behaviour [2, 27, 28, 29, 30]. For the long-range directed transport, interactions between particles are often modelled using an exclusion process on a lattice and analysis is usually based on mean field approximations [27, 31, 32, 33]. Diffusion of particles through a homogeneous medium can be modelled as an unbiased random walk on a discrete lattice or a Brownian motion formulated as a stochastic differential equation (SDE) on a continuous space with spatially homogeneous diffusivity [25]. The time evolution of spatial distribution (or concentration) of particles in association with the SDE is usually described as a drift-diffusion equation in a number of biological applications [34, 35, 36, 37, 38]. Coordinated diffusive and directed transport is usually modelled by a system of partial differential equations (PDEs) (e.g. in [39, 40]) by ignoring interactions of particles.

A previous study of the spatial organization of peroxisomes in living *U maydis* hyphal cells [2] considers a simple 1-D coordinated model to describe the axial placement of three populations of diffusive organelles that are well mixed laterally and coordinated with other two populations (the directed moving organelles).

$$\begin{aligned} \frac{\partial \rho}{\partial t} &= D_{\mathrm{ax}} \frac{d^2\rho}{dx^2} - v\frac{d\rho}{dx} - w_a\rho + w_d(\rho^+ + \rho^-) \\ \frac{\partial \rho^\pm}{\partial t} &= \mp u \frac{d\rho^\pm}{dx} + \frac{w_a}{2}\rho - w_d\rho^\pm - \omega(\rho^\pm - \rho^\mp) \end{aligned} \tag{1}$$

with boundary conditions:

$$\begin{aligned} D_{\mathrm{ax}}\rho_x - v\rho = 0, \quad x = 0, L \\ \rho^+(x) = \rho^-(x), \quad x = 0, L. \end{aligned} \tag{2}$$

This coupled 1-D model is similar to the three-state model for kinesin motor transport in [41] but allows the transition between two directed transport states and poleward drift of diffusive particles. Analytical methods such as the quasi-steady-state (QSS) method [25, 41, 42] under certain conditions have been proposed to reduce and solve these PDEs and have been applied for a wide range of active transport processes.

Models have also been developed to take the heterogeneous environment into account in the diffusion process. For instance, a computational model was implemented to study diffusion in

dendrite-like structures yielding anomalous diffusion [17]. Another geometrically heterogeneous example is diffusion in a narrow 2-D (or 3-D) channel of a varying cross section such as the motion of molecules through carbon nanotubes [43], for which methods have been introduced to project the diffusion into a lower dimensional space with an effective diffusivity [43, 44, 45]. To address the influence of molecular crowding on diffusion, heterogeneity has been modelled in terms of randomly positioned obstacles with the effects of excluded volume [46].

Heterogeneous diffusivity leads naturally to considerations of diffusion processes with discontinuity in diffusion rates (referred as skew diffusion); see e.g. [47, 48]. 1-D skew diffusion process is tractable [49, 50] and several simulation methods have been proposed to simulate its process; see [51] and references therein. Theoretical study of advective skew dispersion has been extended to cases with non-zero drift or multiple layered media [49, 52, 53], and simulation methods have been extended for high-dimensional interface such as hyperplanes and circles [48, 54]. In the presence of drift in diffusion with discontinuity the process can be described by an elastic skew Brownian motion [49].

In this paper, we extend the coupled 1-D transport model (1) to a more realistic (but still idealized) 3-D model that includes heterogeneous and piecewise-constant diffusivity. We focus on steady state distribution of particles and explore conditions where the extended 3-D model are well described by the coupled 1-D model (1) of [2] or even a simplier 1-D scalar model. We explore the efficiency of individual components in our model, in opposing a poleward drift in order to give approximately even equilibrium distribution of organelles within the cell.

2 An idealized 3-D model of coordinated organelle motion within an elongated cell

2.1 A particle-based 3-D model

We present here a model for the transport of organelles within an elongated living cell represented by a cylinder domain $\Omega := \{\mathbf{x} = (x, y, z) : y^2 + z^2 \leq R, 0 \leq x \leq L\}$. The model takes into account the drift diffusion in the cytoplasm and long-range bidirectional transport along MTs. The MTs are allocated in the center of the cell and is organized in an orientation given by a unit vector field $\mathbf{m} := (1, 0, 0)$. Organelles near MTs are assumed to have different diffusivity compared to those far away from MTs as seen in [2]. For simplicity, we consider a zone around MTs (that we call the MT zone) denoted by $\Omega_C := \{(x, y, z) \in \Omega : y^2 + z^2 \leq R_0\}$. With this set up for the MT zone and

the cell geometry (see the cartoon in Fig 1), we make the following assumptions on the transport behaviour:

A1 Diffusive organelles move with a drift velocity $\mathbf{v}$ and diffusivity tensor $\mathbf{D}$, both of which may depend on locations. For simplicity we assume piecewise constant diffusivity which has a discontinuity at the MT zone boundary $\partial\Omega_C$; we denote by $\mathbf{D}^-$ for the diffusivity inside MT zone and by $\mathbf{D}^+$ for that outside the MT zone. The poleward drift of organelles is shown to be mediated by actin-based processes in *U. maydis* [2] and thus we include only one non-zero component - the x-component. We denote $v := \mathbf{v} \cdot \mathbf{m}$ for the non-zero velocity component of drift.

A2 Organelles in the MT zone bind onto MTs at a constant rate w_a (with equal probability for each direction) to move directly along MTs with a mean velocity $\pm u\mathbf{m}$ for each of two directions respectively. We denote "+" for motion towards the tip ($x = L$) and "-" for away from the tip.

A3 Organelles on MTs unbind from the MTs at a constant rate w_d to move diffusively in the cytoplasm.

A4 Organelles on MTs change direction of motion at a constant rate w. At the ends of MT zone (i.e. $\Gamma := \{\mathbf{x} = (x, y, z) \in \Omega_C : x = 0, L\}$), they change direction immediately; this reflects a situation where there is no clustering of organelles at MT ends [2].

A5 The system is in a dilute state, i.e., we do not consider crowding of the organelles that are being transported and we assume particles do not interact with each other.

A6 On the timescale considered, no organelles enter or leave the cell, nor is there production or destruction of organelles. This means that the total amount of organelles is conserved during the transport and there is no net flux of organelles at the cell membrane.

It is noticed in [2] that organelles near MTs diffuse faster than those far away from MTs; this is considered to be the influence of interactions with cargos moving along MTs. Similarly, axial diffusion can be larger than lateral diffusion due to interactions with directed moving cargos along the cell axis, or interactions with actin-based movement near the cell cortex. Thus, we assume different diffusivity for particles within the MT zone compared to those outsize the MT zone and also different diffusivity between axial (i.e. $x-$axis) and lateral (i.e. $y(z)-$axis) diffusivity (denoted as $D_{\text{lat}}, D_{\text{ax}}$ respectively.). For simplicity we assume the diffusion rates to be piecewise constant,

with discontinuity at the interface $\partial\Omega_C$, to model the heterogeneity in the cytoplasm and write the diffusion matrix $\mathbf{D}(\mathbf{x})$ as

$$\mathbf{D}(\mathbf{x}) = \begin{pmatrix} D_{\text{ax}}(\mathbf{x}) & 0 & 0 \\ 0 & D_{\text{lat}}(\mathbf{x}) & 0 \\ 0 & 0 & D_{\text{lat}}(\mathbf{x}) \end{pmatrix}$$

where $D_{\text{ax}}(\mathbf{x}) = D_{ax}^{-}$, $D_{\text{lat}}(\mathbf{x}) = D_{\text{lat}}^{-}$ if $\mathbf{x} \in \Omega_C$ and otherwise $D_{\text{ax}}(\mathbf{x}) = D_{\text{ax}}^{+}$, $D_{\text{lat}}(\mathbf{x}) = D_{\text{lat}}^{+}$ where $D_{\text{ax(lat)}}^{\pm}$ are constants. That is $\mathbf{D}(\mathbf{x}) = \mathbf{D}^{-}$ if $\mathbf{x} \in \Omega_c$ and otherwise $\mathbf{D}(\mathbf{x}) = \mathbf{D}^{+}$.

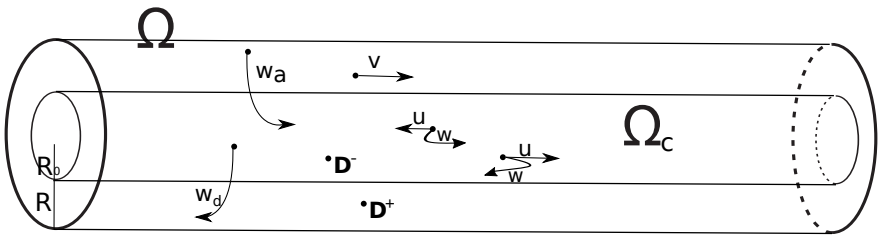

Figure 1: Illustration of a cylindrical geometry for the 3-D coordinated transport model. $\Omega := \{\mathbf{x} = (x, y, z) : y^2 + z^2 \leq R, 0 \leq x \leq L\}$ represents the domain of a cell with length L and radius R; $\Omega_C := \{(x, y, z) \in \Omega : y^2 + z^2 \leq R_0\}$ represents a MT zone with radius R_0 where microtubule-based bi-directed transport occurs with speed u; transition between forward and backward directed movement occurs with rate ω. Particles diffuse with diffusivity $\mathbf{D}^{+}$ when outside Ω_C and with $\mathbf{D}^{-}$ when inside Ω_c. Particles in the MT zone Ω_C leave the zone with rate ω_d and particles outside the MT zone enter into the zone with rate ω_a. Diffusive particles are also assumed to drift with velocity v.

Particle movements are simulated according to a stochastic simulation scheme given in Appendix A. Fig 2 illustrates an example of a particle path simulated within a geometry of $L = 30\mu m$, $R = 0.86\mu m$ and $R_0 = 0.25\mu m$, considering the radius and typical hyphal cell and MT zone inside [2]. This geometry is used throughout the manuscript.

2.2 A dilute population-based 3-D model

With the assumptions A1-A5 in Section 2.1 and an assumption of a dilute population with no interaction, we model the spatial distribution of particles $P(\mathbf{x}, t)$ (i.e., the probability of finding a particle at position $\mathbf{x} \in \Omega$ and time t) using coupled drift-diffusion equations as follows. We classify particles into three populations and denote the density of each population by $\rho(\mathbf{x}, t)$ for drift-diffusive particles and $\rho^{\pm}(\mathbf{x}, t)$ for directed moving particles in an orientation. Thus $P(\mathbf{x}, t) =$

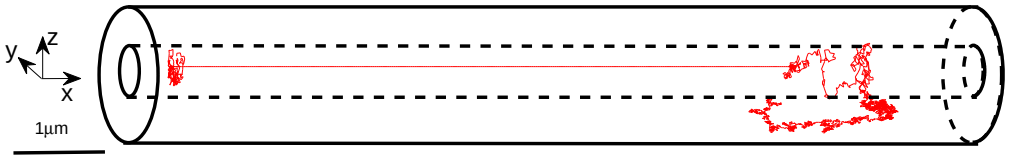

Figure 2: Illustration of a single trajectory simulated in a geometry with $L = 30\mu m, R = 0.86\mu m, R_0 = 0.25\mu m$ for 50s; only a section of the geometry is shown for visualization effect. Diffusion rates used are (in $\mu m^2/s$): $D^-_{\text{lat}} = 0.04$, $D^+_{\text{lat}} = 0.001$, $D^-_{\text{ax}} = 0.015$, $D^+_{\text{ax}} = 0.003$ and other parameters are $u = 1.9\mu m/s$, $v = 4.4 \times 10^{-4}\mu m/s$, $w_a = 0.2/s$, $w_d = 0.17/s$, $\omega = 0.12/s$. Observe how the particle switches from a diffusive motion to a deterministic long range motion in the MT zone and then back to diffusive motion. The deterministic long range motion only occurs if the particle is within the inner cylinder (the MT zone).

$\rho(\mathbf{x}, t) + \rho^+(\mathbf{x}, t) + \rho^-(\mathbf{x}, t)$ and their time evolutions are governed by the following equations:

$$\begin{aligned}
&\tfrac{\partial \rho}{\partial t} = \nabla \cdot \mathbf{J}(\rho), && \mathbf{x} \in \Omega \backslash \Omega_C \\
&\tfrac{\partial \rho}{\partial t} = \nabla \cdot \mathbf{J}(\rho) - (w_a \rho - w_d \rho^+ - w_d \rho^-), && \mathbf{x} \in \Omega_C \\
&\tfrac{\partial \rho^\pm}{\partial t} = \mp u \mathbf{m} \cdot \nabla \rho^\pm + \tfrac{w_a}{2} \rho - w_d \rho^\pm - \omega(\rho^\pm - \rho^\mp), && \mathbf{x} \in \Omega_C
\end{aligned} \tag{3}$$

with boundary conditions:

$$\begin{aligned}
\mathbf{n} \cdot \mathbf{J} = 0, \quad & \forall \mathbf{x} \in \partial\Omega \\
\rho, \mathbf{n} \cdot \mathbf{J} \text{ continuous }, \quad & \forall \mathbf{x} \in \partial\Omega_C \\
J^+ = -J^-, \quad & \forall \mathbf{x} \in \{\Omega_c | x = 0, \text{or}, L\}
\end{aligned} \tag{4}$$

where $\mathbf{J}(\rho) = \mathbf{D}\nabla\rho - \mathbf{v}\rho$ and $J^\pm = \pm u \rho^\pm$. Recall that $\mathbf{D}(\mathbf{x})$ is a piecewise constant function with two constant matrix-valued diffusion rates for $\mathbf{x} \in \Omega_C$ and $\mathbf{x} \in \Omega \backslash \Omega_C$. The first boundary condition refers to the net flux of particles, the second condition requires continuity in the density and flux of particles, while the last condition refers to the immediate return at MT ends in the directed transport. The immediate return (change of population type) of directed moving particles at MT ends corresponds to the observation that their carrier early endosomes typically do not fall off the MT or form cluster at the cell tip, instead they rapidly move away from the tip due to dynein motor activity [13, 29, 2].

Note there is invariance of particle density of each population $\rho(\mathbf{x}), \rho^\pm(\mathbf{x})$ to rotation in the y-z space in the steady state, and so we consider polar coordinates in the cross section. Let $y = r\cos\theta, z = r\sin\theta$, then we have $\frac{d\rho}{d\theta} = \frac{d\rho^\pm}{d\theta} = 0$. Thus in the steady state, the model (3) has a

solution independent of θ that satisfies

$$\begin{aligned}
0 = \;& D^-_{\rm ax}\rho_{xx} + \tfrac{1}{r}\tfrac{\partial}{\partial r}(rD^-_{\rm lat}\rho_r) - v\rho_x && r\in[R_0,R],\ x\in[0,L]\\
0 = \;& D^+_{\rm ax}\rho_{xx} + \tfrac{1}{r}\tfrac{\partial}{\partial r}(rD^+_{\rm lat}\rho_r) - v\rho_x - (w_a\rho - w_d\rho^+ - w_d\rho^-), && r\in[0,R_0],\ x\in[0,L]\\
0 = \;& \mp u\tfrac{\partial\rho^\pm}{\partial x} + \tfrac{w_a}{2}\rho - w_d\rho^\pm + \omega(\rho^\pm - \rho^\mp), && r\in[0,R_0],\ x\in[0,L]
\end{aligned} \tag{5}$$

subject to boundary conditions:

$$\begin{aligned}
&J_{\rm ax} := D_{\rm ax}(r)\rho_x - v\rho = 0, && r\in[0,R], x = 0, L\\
&J_{\rm lat} := D_{\rm lat}\rho_r = 0, && r = R, x\in[0,L]\\
&J_{\rm ax}, J_{\rm lat}, \rho \text{ continuous }, && r = R_0, x\in[0,L]\\
&\rho^+(r,x) = \rho^-(r,x), && r\in[0,R_0], x = 0, L
\end{aligned}$$

where $D_{\rm ax}(r) = D^-_{\rm ax}$, $D_{\rm lat}(r) = D^-_{\rm lat}$ if $r \le R_0$ and otherwise $D_{\rm ax}(r) = D^+_{\rm ax}$, $D_{\rm lat}(r) = D^+_{\rm lat}$. We use the same notation $D_{\rm ax}(\cdot)$, $D_{\rm lat}(\cdot)$ in different coordinates without ambiguity. The corresponding dimensionless equations can be found on setting $\tau = \omega t$, $s = r/R, \xi = x/L$ and $s_0 = R_0/R$, namely

$$\begin{aligned}
0 = \;& \rho_{\xi\xi} + \tfrac{Q^+}{s}\tfrac{\partial}{\partial s}(s\rho_s) - Pe^+\rho_\xi, && s\in[s_0,1],\ \xi\in[0,1]\\
0 = \;& \rho_{\xi\xi} + \tfrac{Q^-}{s}\tfrac{\partial}{\partial s}(s\rho_s) - Pe^-\rho_\xi - (W_a\rho - W_d\rho^+ - W_d\rho^-), && s\in[0,s_0],\ \xi\in[0,1]\\
0 = \;& \mp U\tfrac{\partial\rho^\pm}{\partial\xi} + \tfrac{W_a}{2}\rho - W_d\rho^\pm + \tfrac{1}{\hat D^-_{ax}}(\rho^\pm - \rho^\mp), && s\in[0,s_0],\ \xi\in[0,1]
\end{aligned} \tag{6}$$

where $Pe^\pm := \frac{vL}{D^\pm_{ax}}$, $Q^\pm := \frac{L^2 D^\pm_{lat}}{R^2 D^\pm_{ax}}$, $W_{a,d} := \frac{w_{a,d}L^2}{D^-_{ax}}$, $U := \frac{uL}{D^-_{ax}}$ and $\hat D^-_{ax} := \frac{D^-_{ax}}{\omega L^2}$; see Appendix B. This means the population dynamics arises through a combination of a standard single-species drift-diffusion, coupled to two other populations confined to $s < s_0$ that are of hyperbolic type.

In the following sections, we investigate conditions where the 3-D model (6) or (5) can be reduced to the coupled 1-D model (1) or even a simplier scalar 1-D model and study the importance of individual components in the coordinated transport in opposing drift to evenly distribute particles.

3 Results

3.1 Reduction to the coupled 1-D model

In this section, we examine conditions where the 3-D model (5) could be reduced the 1-D model (1). From dimensionless Eq. (6), when $Q^\pm$ are sufficiently large (i.e. sufficiently large lateral diffusivity $D^\pm_{\rm lat}$), we consider the dependence of ρ, ρ_x on radius r is weak. We take integral over the cross section in Eq. (5) and denote $\tilde\rho(x) = \int_0^R 2\pi r\rho(r,x)dr$, $\tilde\rho^\pm(x) = \int_0^R 2\pi r\rho^\pm(r,x)dr$. By ignoring

the term $\frac{\partial}{\partial r}(r\rho_r)$ in Eq. (5) and dependence on r of ρ, ρ_x, we write the 3-D mode (5) as the 1-D model (1) for $\tilde{\rho}, \tilde{\rho}^{\pm}$ where diffusivity and binding rates are replaced by effective rates expressed as

$$D_{\text{ax,eff}} := D^{-}_{\text{ax}} p + D^{+}_{\text{ax}}(1-p), \quad w_{a,\text{eff}} = p w_a \tag{7}$$

Here $p = \frac{R_0^2}{R^2}$ is the proportion of volume in the inner cylinder Ω_C. Thus the total density profile along the x-axis can be expressed as $\tilde{P}(x) = 2\pi \int_0^R P(r,x) r dr = \tilde{\rho}(x) + \tilde{\rho}^{+}(x) + \tilde{\rho}^{-}(x)$. For convinience, we still denote $P(x)$ as the total density profile along x-axis.

To examine this reduction from 3-D to 1-D model, we compare the total density profile $P(x)$ obtained from the particle-based simulation described in Appendix A with numerically calculated solution of the model (1) using effective rates (7). Fig 3 (a2,d2) show two examples where the 3-D model (5) well reduces to the coupled 1-D model (1) in terms of the density profile $P(x)$ for cases: drift diffusion only with $w_a = 0^{-1}s$ and coupled with directed transport ($\omega_a = 0.0034 s^{-1}$); the corresponding variation on the lateral direction of density profile $\rho(r,x)$ of diffusive particles can be seen in Fig 3 (a1,d1) which show homogeneous density in radius.

To further confirm the validity of the effective rate expression (7), we calculate the effective rates from simulated paths $\mathbf{x}_t$. The simulated effective diffusion rate is calculated by fitting the mean square displacement $MSD(t)$ with a time lag t in longitude direction to the linear function $MSD(t) = 2Dt$ in a short time scale. The effective binding rate is calculated as the inverse of simulated mean first binding time to the MT. The mean binding time takes averages over a number of initially evenly-distributed particles in the domain Ω. We remark here that the first binding time is not simply a combination of first entering time to the MT zone and its waiting time to bind onto MTs, as a particle within the MT zone could diffuse out of the zone before it has a chance to bind. Fig 4 shows that the simulated effective rates indeed agree with the analytical expression (7) for various MT zone radius.

We calculate the difference of total density profiles $P(x)$ between 3-D model and 1-D model reduction (1) using effective diffusion and binding rates from (7), on varying Pe^{+} and Q^{+} for fixed Pe^{-} and Q^{-}, and show this in Fig 3 (c,f). The difference is calculated using the L_1 metric $|P'(x) - P(x)|_1 := \int_0^L |P'(x) - P(x)| dx$ where $P(x)$ and $P'(x)$ are total density profiles from 3-D model simulations and 1-D model calculations respectively. Indeed, we see from Fig 3 (c,f) that with larger Q^{+}, the total density profile $P(x)$ from 1-D model reduction gets closer to the total density profile from 3-D model simulation, meaning that given sufficiently large Q^{-} and Q^{+}, the 3-D model can be reduced to 1-D model with effective rates (7). In terms of diffusivity, this indicates for fixed axial diffusivity, sufficiently large lateral diffusivity allows the reduction of the 3-D model (5) to the 1-D model (1) with effective rates given in (7).

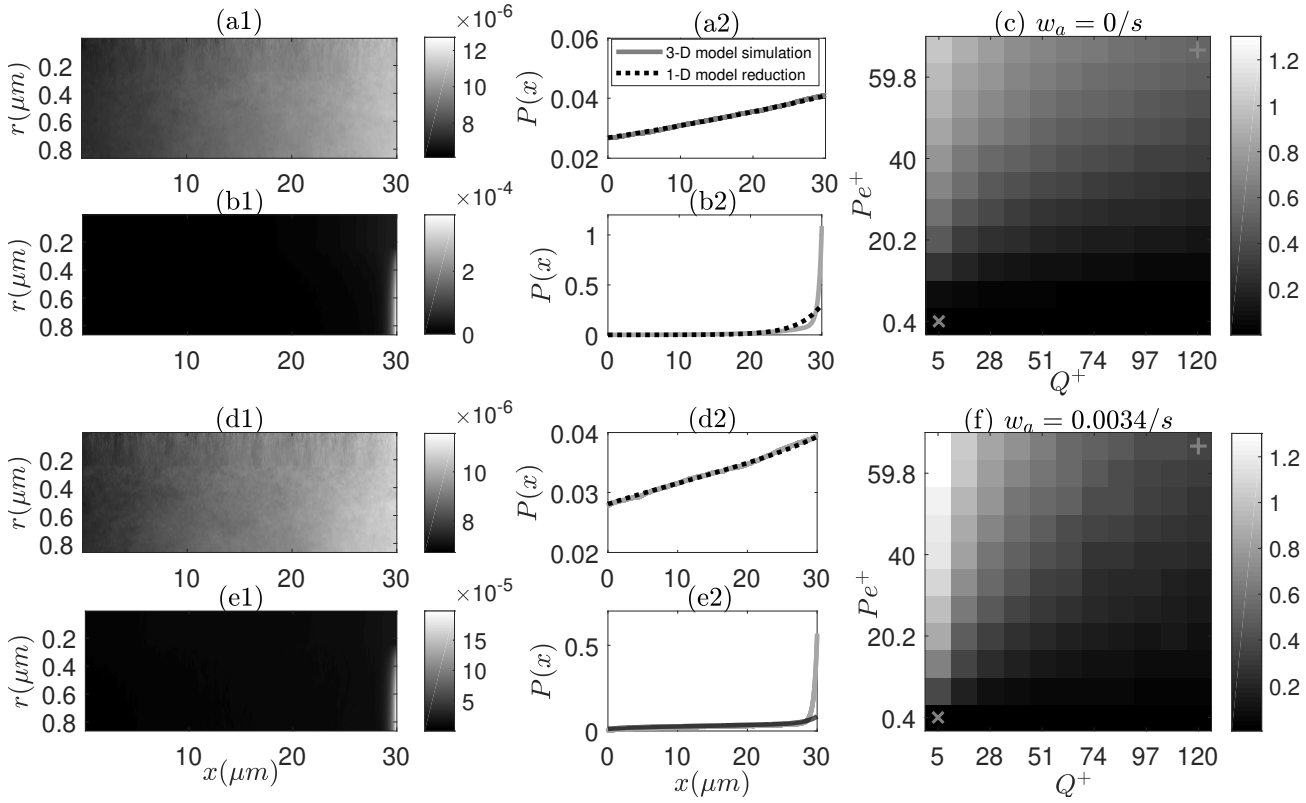

Figure 3: The panels show density profile $\rho(r, x)$ for the diffusive population (left panels), total density profiles of all populations $P(x)$ (middle panels) and the difference (right panels) of the total density profiles $P(x)$ between simulations of the 3-D model (3) and numerical calculations of the reduced 1-D model (1) with effective diffusion and binding rates from (7). The difference on $P(x)$ is calculated as L_1 metric. Note that the total density profile $P(x) = 2\pi \int_0^R r(\rho(r, x) + \rho^+(r, x) + \rho^-(r, x))dr$ is conserved as $\int_0^L P(x) = 1$. The top panels (a-c) show for $w_a = 0/s$ while bottom panels (d-f) show for $w_a = 0.0034\ s^{-1}$. (a1-a2) use parameters $Pe^+ = 0.4$ and $Q^+ = 5$ which corresponds to $D^+_{\text{lat}} = 2.7 \times 10^{-4}\mu m^2/s$, $D^+_{\text{ax}} = 3.15 \times 10^{-2}\mu m^2/s$, and $w_a = 0/s$. The difference on $P(x)$ between 3-D model and 1-D model is marked '×' in (c). (b1-b2) use parameters $Pe^+ = 66.4$, and $Q^+ = 120$ which corresponds to $D^+_{\text{lat}} = 3.9 \times 10^{-5}\mu m^2/s$, $D^+_{\text{ax}} = 1.4 \times 10^{-3}\mu m^2/s$, and $w_a = 0/s$. The difference on $P(x)$ is marked '+' in (c). (d1-d2) use parameters the same as in (a1,a2) except that $w_a = 0.0034/s$. The difference on $P(x)$ is marked '×' in (f). (e1-e2) use parameters the same as in (b1,b2) except that $w_a = 0.0034/s$. The difference on $P(x)$ is marked '+' in (f). Simulated densities are averaged over 2×10^{10} steps. Other parameters if unspecified are $v = 4.4 \times 10^{-4}\mu m/s$, $w_d = 0.17/s$, $w = 0.12/s, u = 1.9\mu m/s$, $D^-_{\text{lat}} = 1.4 \times 10^{-3}\mu m^2/s$, $D^-_{\text{ax}} = 0.015\mu m^2/s$ (which correspond to $Pe^- = 0.88$ and $Q^- = 113$).

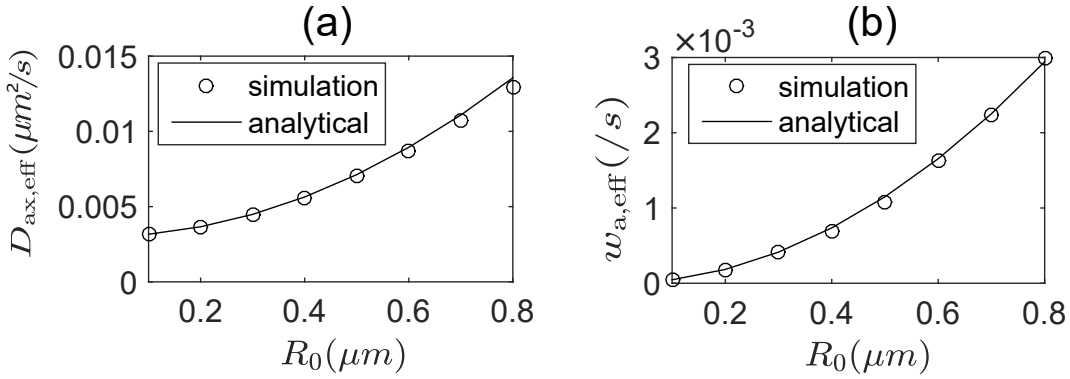

Figure 4: Illustration of effective axial diffusion rate (a) and binding rate (b) on varying radius R_0. Effective binding and axial diffusion rates from 3-D model simulations agree well with the analytical approximation (7). (a) uses parameters $v = 0\mu m/s$, $w_a = 0/s$, $D^-_{\mathrm{lat}} = 1.4\times 10^{-3}\mu m^2/s$ and (b) uses parameters $w_a = 3.4 \times 10^{-3}/s$, $D^-_{\mathrm{lat}} = 4.2 \times 10^{-3}\mu m^2/s$. In both panels $D^+_{\mathrm{lat}} = 1.4 \times 10^{-3}\mu m^2/s$, $D^-_{\mathrm{ax}} = 0.015\mu m^2/s$, $D^+_{\mathrm{ax}} = 3 \times 10^{-3}\mu m^2/s$ and other parameters are the same as in Fig 3 (d2). In panel (b), the corresponding $Pe^- = 0.88$, $Q^- = 341$, $Pe^+ = 4.4$, $Q^+ = 568$.

Fig 3 (b2,e2) shown two examples when Q^+ is no longer sufficiently large that the 3-D model (5) cannot be well reduced to 1-D model (1) with the effective rates given in (7) for cases with/without directed transport. In such cases the density profile $\rho(r, x)$ has sharp gradient in radius as shown in Fig 3 (b1,e1). We also test the effective binding rate expression (7) in Fig 5. When Q^+ is no longer sufficiently large, the simulated effective binding rate deviates from the value given by (7). In particular, decreasing Q^+ (i.e. decreasing D^+_{lat}), the simulated effective binding rate gets further away from (7) as seen from Fig 5.

3.2 Reduction via QSS to a scalar 1-D model

In this section, we consider parameters where the reduced coupled 1-D model (1) can be further reduced to a scalar 1-D model of the total density profile along cell axis via QSS approximation. The QSS reduction is based on the method described by Newby and Brossloff [42] and assumes that the timescale associated with transitions between particle populations is short relative to the time taken for particles to move across the cell. Explicitly, we consider when transitions occurs much faster than movement (i.e. $\omega, w_{a,d} \gg \frac{\max\{u,v\}}{L}$). We set $t \to \frac{tu}{L}$ and $x \to \frac{x}{L}$. The rescaled system of Eq. (1) can be written as

$$\begin{aligned} \frac{\partial \rho^{\pm}}{\partial t} &= \mp \frac{\partial \rho^{\pm}}{\partial x} + \frac{w_a L}{2u}\rho - \frac{w_d L}{u}\rho^{\pm} + \frac{\omega L}{u}(\rho^{\pm} - \rho^{\mp}), \quad x \in [0,1] \\ \frac{\partial \rho}{\partial t} &= \frac{D_{\mathrm{ax}}}{uL}\rho_{xx} - \frac{v}{u}\rho_x - \frac{w_a L}{u}\rho + \frac{w_d L}{u}(\rho^+ + \rho^-), \quad x \in [0,1] \end{aligned} \tag{8}$$

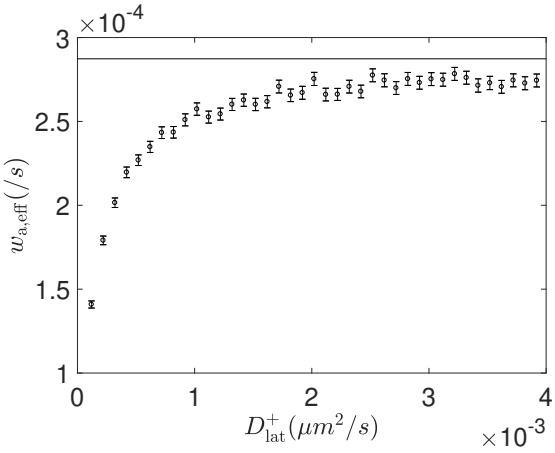

Figure 5: Left: effective binding rate calculated from the mean first binding time from 3-D model simulations of paths. The line gives value from expression (7). $D^-_{\mathrm{lat}} = 1.4 \times 10^{-3}\mu m^2/s$. Other parameters are the same as in Fig 3 (d2). The corresponding $Pe^- = 0.88$, $Q^- = 113$, $Pe^+ = 4.4$. Q^+ decreases from 162 to 40 when D^+_{lat} decreases from $4 \times 10^{-3}\mu m^2/s$ to $1 \times 10^{-4}\mu m^2/s$.

Then there exist $\epsilon \ll 1$ such that transition rates $\frac{w_{a,d}L}{u}, \frac{\omega L}{u}$ are of order $O(1/\epsilon)$. Following from [41, 42], we write in a matrix form as

$$\frac{\partial \mathbf{p}}{\partial t} = \frac{1}{\epsilon} A\mathbf{p} + M(\mathbf{p}) \tag{9}$$

where $\mathbf{p} = (\rho^+, \rho^-, \rho)^T$ is a state vector, A is a modified transition matrix of order 1, and M is a differential operator for the spatial derivatives and can be written as a matrix with zeros off the diagonal and diagonal entries $M_{ii} = -v_i\partial_x + D_i\partial_x^2$; here $v_1 = 1, v_2 = -1, v_3 = v/u$, $D_1 = D_2 = 0, D_3 = \frac{D_{ax}}{uL}$, and

$$A = \begin{pmatrix} -\frac{\epsilon(w_d+\omega)L}{u} & \frac{\epsilon\omega L}{u} & \frac{\epsilon w_a L}{2u} \\ \frac{\epsilon\omega L}{u} & -\frac{\epsilon(w_d+\omega)L}{u} & \frac{\epsilon w_a L}{2u} \\ \frac{\epsilon w_d L}{u} & \frac{\epsilon w_d L}{u} & -\frac{\epsilon w_a L}{u} \end{pmatrix}. \tag{10}$$

Matrix A has one zero eigenvalue with the corresponding normalized eigenvector

$$\mathbf{P^{ss}} := \frac{w_d}{w_a + w_d}(\frac{w_a}{2w_d}, \frac{w_a}{2w_d}, 1)^T$$

such that $\Psi^T\mathbf{P^{ss}} = 1$ (here the vector $\Psi = (1, 1, 1)^T$). Using the quasi-steady approach [41], assuming diffusivities are of order $O(\epsilon)$, the equation for total particle density $P(x, t)$ to the order of ϵ can be approximated as

$$\partial_t P = -V\partial_x P + D\partial_x^2 P, \quad x \in [0, 1] \tag{11}$$

with boundary conditions: $VP - DP_x = 0, x = 0, 1$, where $V = \langle v \rangle = \frac{v}{u}\frac{w_d}{w_a+w_d}$ and $D = \langle D \rangle + \epsilon \mathbf{v}^T\theta = \frac{w_d D_{ax}}{uL(w_a+w_d)} + (\frac{1}{2\omega+w_d} + \frac{v^2 w_d}{u^2(w_a+w_d)^2})\frac{uw_a}{L(w_a+w_d)}$ (see Appendix C for details). Here $\langle\cdot\rangle$ is a weighted mean, using entries of the vector $\mathbf{P}^{ss}$ as the weights. The solution in the original space $[0, L]$ is then

$$P(x) = \gamma \exp(\frac{Vx}{DL}), x \in [0, L] \tag{12}$$

where γ is a normalization such that $\int_0^L P(x) = 1$. Fig C.1 shows an example of particle total density distribution calculated from analytical solution (12) that agrees well to numerical calculation of the Eq. (1) in steady state.

3.3 Mechanisms that oppose poleward drift

An even distribution of organelles such as peroxisomes and lipid droplets is critical to their role in lipid and reactive oxygen species homeostasis [2]. Mechanisms underlying even distribution remain elusive. With quantitative information from [2], it was shown that directed transport and, to a lesser degree diffusion, contributes to overcoming the poleward drift to ensure an "even" distribution of organelles. In this section, we further study mechanisms underlying even distribution of particles by quantitative analysis of effects from individual model components.

For a spatial distribution $P(x)$, we use the L_1 metric distance to characterize its difference to the even distribution $\Theta(x) = 1/L$ ($x \in [0, L]$). This distance ranges over $[0, 2)$. We say that the axial distribution $P(x)$ is approximately even if $|\Theta - P|_1$ is sufficiently small. It was shown that peroxisomes are approximately in an even distribution [2]. Assuming organelles are well mixed in lateral diffusion, and using experimentally estimated poleward drift velocity, directed transport speed and effective transition rates (as in Fig 3(d2)) together with effective axial diffusivity $D_{\text{ax}} = 0.015\mu m^2/s$ [2], the model gives axial particle density $P(x)$ with a distance $|\Theta - P|_1 = 0.025$ for peroxisomes in wild type cells. When cells are treated with a MT-depolymerizing drug (where directed transport was blocked, i.e. $\omega_a = 0/s$), the effective axial diffusivity was measured as $D_{\text{ax}} = 0.003\mu m^2/s$ [2]; together with estimated drift velocity, the model gives $|\Theta - P|_1 = 0.86$. This is far from even; in fact, the peroxisomes clusters at the cell tip under such treatment. In the following, we explore contribution of individual parameters in overcoming poleward drift.

Firstly, we consider the case where the 3-D coordinated transport model can be reduced to the coupled 1-D model (1). We still denote D_{ax} and w_a for the effective diffusion and binding rates respectively without ambiguity. We investigate the importance of individual components (directed velocity, turning, binding, unbinding, and diffusivity) in overcoming increased drift. To compare the effects of individual components in opposing polar drift, we choose a reference parameter set

that gives total density profile P such that $d = |\Theta - P|_1 \approx 0.025$, and then calculate their minimum changes of individual parameters relative to the reference value for an increased drift, in order to maintain its distribution $P'(x)$ such that $|\Theta - P'|_1 = d$. For instance, for an increased drift, we change parameter u to u' while remaining other parameters unchanged such that the new spatial distribution $|P' - \Theta| = d$ and refer the minimum change u'/u (if possible) as multiplicative factor for the parameter u. A multiplicative factor larger (less) than 1 indicates the required increase (decrease) of the corresponding parameter to overcome an increased drift.

In the case $w_a = 0$ and $w_d > 0$, particles eventually undergo drift diffusion in cytoplasm, and the system (1) reduces to

$$0 = -v\frac{d\rho}{dx} + D_{\text{ax}}\frac{d^2\rho}{dx^2}, \rho^{\pm} \equiv 0 \tag{13}$$

with boundary conditions $-v\rho + D_{\text{ax}}\rho_x = 0$ at $x = 0, L$. This leads to the steady state solution $\rho(x) = \gamma e^{vx/D_{\text{ax}}}$ where γ is a normalization factor. Note that $\omega_d > 0$ is assumed to ensure steady state solution independent of initial conditions. The distance to even distribution is then

$$|\Theta - P|_1 = 2\frac{\ln(\frac{e^c-1}{c}) - 1}{c} + \frac{2}{e^c - 1} \tag{14}$$

where $c = Lv/D_{\text{ax}}$ is the Péclet number. This distance increases with increasing c (also v for fixed D_{ax}) and the speed of increase slows down with increasing c. Thus, for drift-diffusion only systems, in order to reach approximately-even distribution of peroxisomes, a large diffusivity is required to oppose the drift. In particular, using estimated poleward drift velocity, a diffusivity of $0.15\mu m^2/s$ (i.e. 50 times larger than that measured in treated cells $D_{ax} = 0.003\mu m^2/s$) is required to overcome the poleward drift and reach a distance $|\Theta - P|_1 = 0.025$ from Eq. (14).

If the transition between modes of transport is much faster than deterministic movement, i.e rates w_d, w_a, ω are much larger than $\frac{\max\{u,v\}}{L}$, we can approximate the system (1) by the QSS method [25, 41] to a scalar system (11), giving the overall density profile (12). This gives an effective Péclet number as

$$Pe = \frac{vw_dL}{D_{ax}w_d + \frac{u^2w_a}{2\omega+w_d} + \frac{w_aw_dv^2}{(w_a+w_d)^2}}. \tag{15}$$

A reference parameter set that give total density profile close to even distribution with distance $d = |\Theta - P|_1 \approx 0.025$, corresponds to an effective Péclet number $Pe \approx 0.1$ from distance (14). For increasing drift velocity, we calculate the multiplication factor for individual parameters (including directed velocity, (un)binding rates, turning rate and axial effective diffusion rate) using effective Péclet number approximation (15) and show this in Fig. 6. From Fig 6, we see that increasing diffusivity, directed velocity or binding rate, or reducing unbinding/turning rates can overcome increased drift to give an approximately even distribution. Reducing unbinding or turning rates,

allows particles to stay and move longer time on tracks. Moreover, we see in Fig 6 that enhance directed moving transport (in particular, the directed moving velocity) is relatively more efficient to overcome increased drift than increasing diffusivity. We also notice that reducing turning rate has limited capability to overcome increased drift; for large drift velocity, reducing turning rate is not able to reach approximately even distribution.

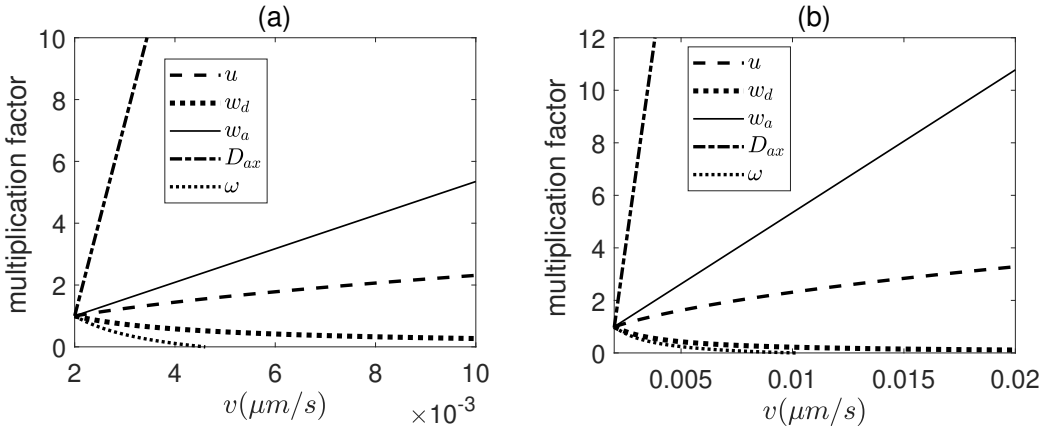

Figure 6: The multiplicative factor for individual parameters relative to reference parameter values, calculated from $|\Theta - P|_1 = 0.025$ in Eq. (14) where the Péclet number is approximation as in Eq. (15). (a) uses reference parameters: $w_a = 1/s$, $w_d = 1.7/s$, $\omega = 1.2/s$, $u = 2\mu m/s$, $D = 0.05\mu m^2/s$ while (b) uses reference parameters: $w_a = 3/s$, $w_d = 1/s$, $\omega = 2.2/s$, $u = 1\mu m/s$, $D = 0.05\mu m^2/s$.

If one or more of the transition rates w_d, w_a, ω is much smaller than $\frac{\max\{u,v\}}{L}$, then the assumptions for QSS reduction method in [25] are no longer satisfied. In particular for observed peroxisome movement in *U maydis*, the experimentally estimated effective binding rate of peroxisomes $\omega_a = 0.0034/s$ is much lower than other transition rates (e.g $w_d = 0.17/s, w = 0.12/s$) and directed movement ($u/L = 0.063/s$). We calculate the total density profile using numerical calculation of the 1-D model (1). We take estimated drift velocity, directed transport speed and effective transition rates (the same as in Fig 3(d2)) together with $D = 0.015\mu m^2/s$ as a reference parameter set and show in Fig 7(a) the multiplication factor for each parameter in order to reach approximately even distribution. Similar to the case shown in Fig 6, we see from Fig 7(a) that by decreasing the turning rate w (only for limited increase of drift velocity), or the unbinding rate w_d, or increasing the diffusivity D_{ax}, the directed velocity u, or the binding rate w_a, particles can overcome drift to achieve an approximately even distribution. In contrast to other components, it is more efficient to increase the directed velocity u or the binding rate ω_a than other components (e.g. turning rate w, unbinding rate ω_d and diffusivity D_{ax}) to enhance the even distribution. This

still holds for reference parameter set with a smaller order of effective diffusivity (Fig 7(b)). For a reference parameter set with a smaller order of effective binding rate $w_a \sim O(10^{-4})$, increasing directed transport speed u is no longer among the most efficient components in overcoming drift (Fig 7(c-d)); besides effective binding rate, increasing effective diffusivity becoming efficient as well to overcome drift. However, note that in the 3-D model, effective diffusivity (7) is the weighted average of axial diffusivity inside D_{ax}^{-} and outsize the zone D_{ax}^{+}. Regarding individual diffusivity $D_{\text{ax}}^{\pm}$, it would then be less efficient than the effective diffusivity. Overall, the effective binding rate in general is a key mechanism in opposing poleward drift to reach approximately even distribution.

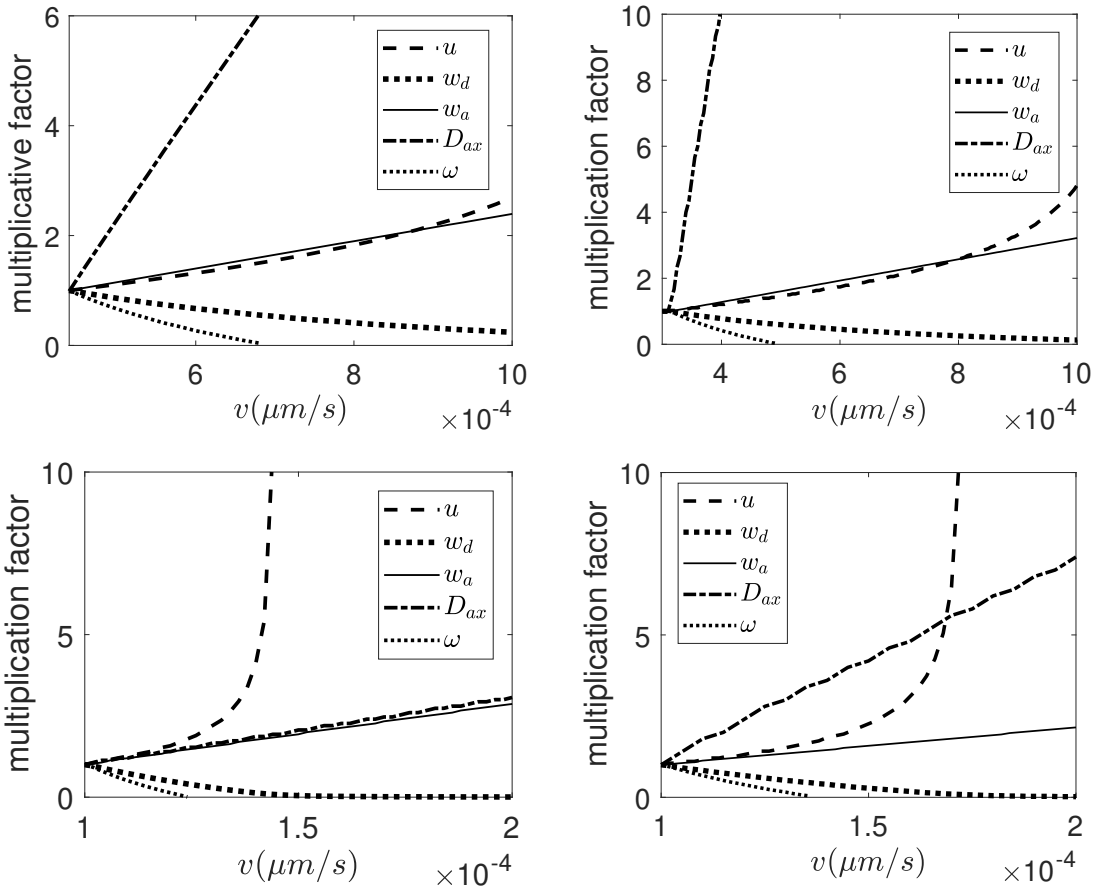

Figure 7: The multiplicative factor for the parameters relative to those measured in experiment to overcome large drift to reach a distance $|\Theta - P|_1 = 0.025$. The reference experimental estimated parameters are: (a)$w_a = 0.0034/s$, $w_d = 0.17/s$, $\omega = 0.12/s$, $D = 0.015\mu m^2/s$, $u = 1.9\mu m/s$. (b)$w_a = 0.003/s$, $w_d = 0.2/s$, $\omega = 0.11/s$, $D = 0.003\mu m^2/s$, $u = 1.9\mu m/s$. (c)$w_a = 0.0003/s$, $w_d = 0.1/s$, $\omega = 0.11/s$, $D = 0.015\mu m^2/s$, $u = 1.9\mu m/s$. (d)$w_a = 0.00046/s$, $w_d = 0.1/s$, $\omega = 0.1/s$, $D = 0.005\mu m^2/s$, $u = 1.9\mu m/s$.

Next, we consider cases where the 3-D model is not well approximated by the reduced 1-D

model (1) with effective rates given in (7). To examine the importance of individual parameters, we simulate the particle paths to get its spatial distribution. We consider an increased drift velocity of $8.8 \times 10^{-4} \mu m/s$ (i.e. two times of that experimentally estimated poleward drift) which cluster particles at one end of the cell. We then increase or reduce (e.g. for the parameter w_d) individual parameters by 5 times or 10 times when keeping other parameters the same, and calculate the difference (L_1 distance) to an even distribution. The differences of total density profiles to the even distribution are shown in Fig 8 for two sets of reference parameters with different binding rates: $w_a = 0.034/s$ in panels (a1-a3) and $w_a = 0.0034/s$ in panels (b1-b3). In the case with equally large lateral diffusivity inside and outside the MT zone, particle density from the 3-D model can be well approximated from 1-D model, and as expected the binding rate is more efficient than other model components; see Fig.8 (a1,b1). When either lateral diffusivity ($D^+_{\rm lat}$ or $D^-_{\rm lat}$) is significantly small (i.e. either Q^+ or Q^- is no longer sufficiently large), Fig.8 (a2-b3) show that enhancing the axial diffusivity outside the zone $D^+_{\rm ax}$ becomes efficient. This is probably due to that with increased axial diffusivity outside the zone, it efficiently reduces the cluster and thus leads to a more even distribution, in particular when the reference binding rate is small (Fig.8 (b2-b3)). Moreover, when lateral diffusivity within the zone $D^-_{\rm lat}$ is significantly small, from Fig. 8(a3) and Fig. 8(b3) we note that increasing the binding rate is also effective to overcome poleward drift, in particular when the reference binding rate is relative large (Fig. 8(a3)).

4 Discussion and further considerations

The 3-D model introduced in Section 2.1 includes for cooperation between MT-mediated long-range bidirectional transport and heterogeneous drift-diffusion of particles in the cytoplasm. It is motivated by observations in living cells of the fungus *U. maydis*, which serves as a model system for long-range membrane trafficking [55, 56, 28].

The 3-D model introduced includes lateral motility of particles and heterogeneous diffusion representing the presence of a more active mixing of organelles near MTs. We study the influence of heterogeneous diffusivity on the particle distribution, and present parameter regions where the reduction to 1-D model can be achieved using effective rates; reduction to a 1-D model allows convenient analytical analysis of system properties and further reduction (e.g. using QSS) may be possible under certain parameter conditions.

Moreover, we study the efficiency with which individual parameters of the model can be used to oppose poleward drift and drive the distribution back towards even.. We find that if lateral motion is well mixed, then increasing the binding rate is efficient, whereas if lateral motion is not

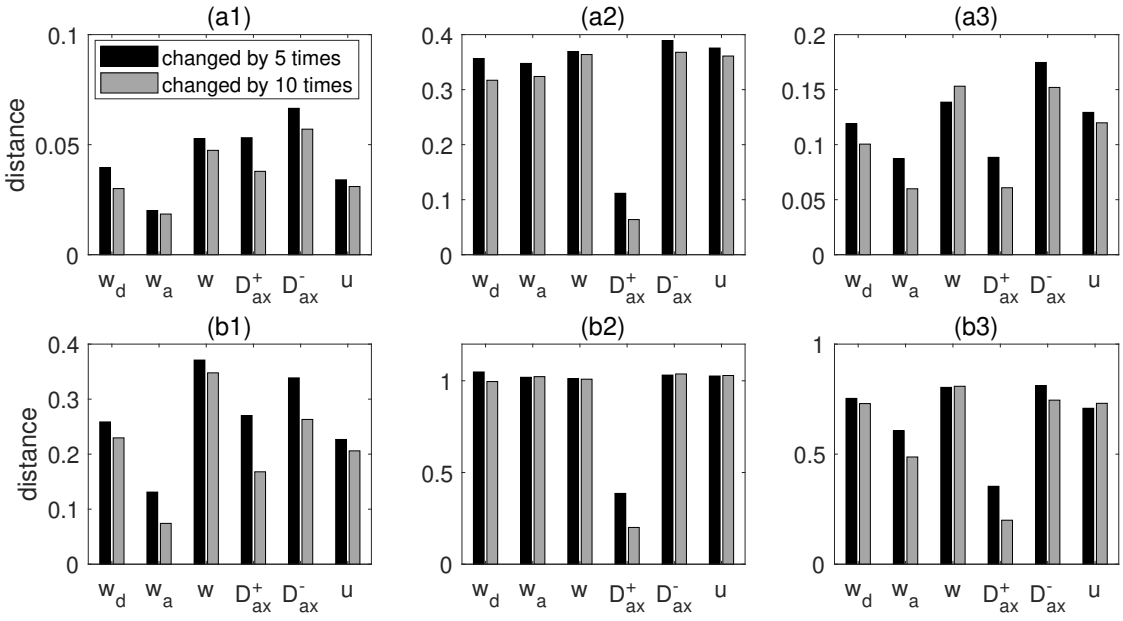

Figure 8: Bars show the difference of particle total density $P(x)$ from 3-D model simulation to the even distribution when the parameter is increased (for $w_a, D^{\pm}_{\text{ax}}$, u) or reduced (for w_d, ω) by 5 (10) times for an increased different drift velocity $v = 8.8 \times 10^{-4}\mu/s$. The reference sets of parameters are: (a1-b1) using homogeneous lateral diffusivity $D^{+}_{\text{lat}} = D^{-}_{\text{lat}} = 1.4 \times 10^{-3}\mu m^2/s$; (a2-b2) using $D^{+}_{\text{lat}} = 1.4 \times 10^{-6}\mu m^2/s$, $D^{-}_{\text{lat}} = 1.4 \times 10^{-3}\mu m^2/s$; (a3-b3) using $D^{+}_{\text{lat}} = 1.4 \times 10^{-3}\mu m^2/s$, $D^{-}_{\text{lat}} = 1.4 \times 10^{-6}\mu m^2/s$. Other parameters in reference are $w_a = 0.034/s$ for panels (a1-a3) ($w_a = 0.0034/s$ for panels (b1-b3)), $w_d = 0.17/s$, $u = 1.9\mu m/s$, $\omega = 0.12/s$, $D^{-}_{\text{ax}} = 0.015\mu m^2/s$, $D^{+}_{\text{ax}} = 3 \times 10^{-3}\mu m^2/s$.

well mixed, then increasing the diffusivity outside the MT zone becomes more efficient to overcome drift. This analysis gives indications of the roles of key mechanisms that can contribute to evenly distribute organelles within a cell.

We remark that our model should be adaptable to help understand transport in similar elongated cells such as neuronal cells [57, 58]. Vesicles of various size in neuronal cells have been shown to be transported by coordinated diffusive and directed transport [4]; microtubule-associated protein tau in neuronal cells has also been modelled as a coordinated transport process [59] in one dimension along MTs. Modelling the coordinated transport in elongated cells takes advantage of its relative simple geometry.

Possible adaptations and extensions include more complicated geometric domains such as transport in mammalian cells where the MTs forms a more complicated network, or including crowding effects for organelles that are not dilute. In-depth understanding of the organization of mam-

malian MT cytoskeleton and roles of motor proteins in intracellular transport will help meeting this challenge.

Acknowledgements

This work was supported by the Biotechnology & Biological Sciences Research Council (BB/J009903/1 to G.S.). The author C.L. also acknowledges financial support from National foundation of Science in China (NFSC, grant No. 11701201 and No. 11871061).

References

[1] Schrader M, Godinho Luis F, Costello Joseph L, and Islinger M. 2015. The different facets of organelle interplay—an overview of organelle interactions. *Front Cell Dev Biol.* **3** 56.

[2] Lin C, Schuster M, Guimaraes S C, Ashwin P, Schrader M, Metz J, Hacker C, Gurr S and Steinberg G 2016 Active diffusion and microtubule-based transport oppose myosin forces to position organelles in cells. *Nat. Commun.* **7** 11814.

[3] Lagache T, Dauty E and Holcman D 2009 Physical principles and models describing intracellular virus particle dynamics. *Curr. Opin. Microbiol.* **12** 439-445.

[4] Ahmed W W and Saif T A 2014 Active transport of vesicles in neurons is modulated by mechanical tension. *Sci. Rep.* **4** 4481.

[5] Bressloff P C and Kim H 2018 Bidirectional transport model of morphogen gradient formation via cytonemes. *Physi. Biol.* **15** 026010.

[6] Vale R D 2003 The molecular motor toolbox for intracellular transport. *Cell* **112** 467-480.

[7] Manneville J-B, Etienne-Manneville S, Skehel P, Carter T, Ogden D and Ferenczi M 2003 Interaction of the actin cytoskeleton with microtubules regulates secretory organelle movement near the plasma membrane in human endothelial cells. *J. Cell Sci.* **116** 3927-3938.

[8] Wang X, Teng Y, Wang Q, Li X, Sheng X, Zheng M, Samaj J, Frantisek B and Lin J 2006 Imaging of dynamic secretory vesicles in living pollen tubes of Picea meyeri using evanescent wave microscopy. *Plant physiol.*. **141** 1591-1603.

[9] Trong P K, Guck J and Goldstein R E 2012 Coupling of active motion and advection shapes intracellular cargo transport. *Phys. Rev. Lett.* **105** 1-5.

[10] Vaccario G, Antoine C, and Talbot J. 2015 First-Passage Times in d-Dimensional Heterogeneous Media. *PRL* **115** 240601.

[11] Smith D. A. and Simmons R. M. 2001. Models of Motor-Assisted Transport of Intracellular Particles. *Biophys. J* **80** 45-68.

[12] Hafner A E, and Rieger H. 2018. Spatial Cytoskeleton Organization Supports Targeted Intracellular Transport. *Biophys. J.* **114** 1420–1432.

[13] Schuster M, Kilaru S, Fink G, Collemare J, Roger Y and Steinberg G 2011 Kinesin-3 and dynein cooperate in long-range retrograde endosome motility along a nonuniform microtubule array. *Mol. Biol. Cell.* **22** 3645-3657.

[14] Schuster M, Lipowsky R, Assmann M-A, Lenz P and Steinberg G 2011 Transient binding of dynein controls bidirectional long-range motility of early endosomes. *Proc. Natl. Acad. Sci. USA* **108** 3618-3623.

[15] Brangwynne C P, Koenderink G H, MacKintosh F C and Weitz D A 2009 Intracellular transport by active diffusion. *Trends Cell Biol.* **19** 423-427.

[16] Otten M, Nandi A, Arcizet D, Gorelashvili M, Lindner B and Heinrich D 2012 Local motion analysis reveals impact of the dynamic cytoskeleton on intracellular subdiffusion. *Biophys. J.* **102** 758-768.

[17] Santamaria F, Wils S, De Schutter S and Augustine G J 2006 Anomalous diffusion in Purkinje cell dendrites caused by spines. *Neuron* **52** 635-648.

[18] Smelser A M, Macosko J C, O'Dell A P, Smyre S, Bonin K and Holzwarth G 2015 Mechanical properties of normal versus cancerous breast cells. *Biomech. Model Mechanobiol.* **14** 1335-1347.

[19] Guo M, Ehrlicher A J, Jensen M H, Renz M, Moore J R, Goldman R D, Lippincott-Schwartz J, Mackintosh F C and Weitz D A 2014 Probing the stochastic, motor-driven properties of the cytoplasm ssing force spectrum microscopy. *Cell* **158** 822-832.

[20] Han D S, Korabel N, Chen R, Johnston M, Allan V J, Fedotov S, Waigh T A 2020 Deciphering anomalous heterogeneous intracellular transport with neural networks. *eLife* **9** e52224.

[21] Witzel P, Götz M, Lanoiselée Y, Franosch T, Grebenkov D S, Heinrich D 2019 Heterogeneities Shape Passive Intracellular Transport. *Biophys. J.* **117** 203-213.

[22] Kulić I M, Brown A E X, Kim H, Kural C, Blehm B, Selvin P R, Nelson P C, Gelfand V I 2008 The role of microtubule movement in bidirectional organelle transport. *Proc. Natl. Acad. Sci. U. S. A.* **105** 10011-10016.

[23] Klumpp S and Lipowsky R 2005 Active Diffusion of Motor Particles. *Phys. Rev. Lett.* **95** 268102.

[24] Drechsler M, Giavazzi F, Cerbino R and Palacios I M 2017 Active diffusion and advection in Drosophila oocytes result from the interplay of actin and microtubules. *Nat. Commun.* **8** 1520.

[25] Bressloff P and Newby J 2013 Stochastic models of intracellular transport. *Rev. Mod. Phys.* **85** 135-196.

[26] Higuchi Y, Ashwin P, Roger Y, Steinberg G. 2015. Early endosome motility spatially organizes polysome distribution. *J Cell Biol.* **204**(3):343-57.

[27] Ashwin P, Lin C and Steinberg G 2010 Queueing induced by bidirectional motor motion near the end of a microtubule. *Phys. Rev. E* **82** 051907.

[28] Higuchi Y, Ashwin P, Roger Y and Steinberg G 2014 Early endosome motility spatially organizes polysome distribution. *J. Cell Biol.* **204** 343-357.

[29] Schuster M, Kilaru S, Ashwin P, Lin C, Severs N J and Steinberg G 2012 Controlled and stochastic retention concentrates dynein at microtubule ends to keep endosomes on track. *EMBO J* **30** 652-664.

[30] Lin C and Steinberg G 2017 Spatial organization of organelles in fungi: Insights from mathematical modelling. *Fungal Genet. Biol.* **103** 55-59.

[31] Lin C, Ashwin P and Steinberg G 2013 Motor-mediated bidirectional transport along an antipolar microtubule bundle: a mathematical model. *Phys. Rev. E* **87** 052709.

[32] Greulicha, P and Santen, L. 2010. Active transport and cluster formation on 2D networks. *Eur. Phys. J. E* **32** 191–208.

[33] Lipowsky R, Klumpp S and Nieuwenhuizen T M 2001 Random walks of cytoskeletal motors in open and closed compartments. *Phys. Rev. Lett.* **87** 108101.

[34] Codling E A, Plank M J and Benhamou S 2008 Random walk models in biology. *J. R. Soc. Interface* **5** 813-834.

[35] Sturrock M, Terry A J, Xirodimas D P, Thompson A M and Chaplain M A J 2011 Spatio-temporal modelling of the Hes1 and p53-Mdm2 intracellular signalling pathways. *J. Theor. Biol.* **273** 15-31.

[36] Grigolon S, Sollich P and Martin O C 2015 Modelling the emergence of polarity patterns for the intercellular transport of auxin in plants. *J. R. Soc. Interface* **12** 20141223.

[37] Bressloff P C and Maclaurin J N 2018 Stochastic Hybrid Systems in Cellular Neuroscience. *J. Math. Neurosci.* **8** 12.

[38] Peletier M A, Westerhoff H V and Kholodenko B N 2003 Control of spatially heterogeneous and time-varying cellular reaction networks: a new summation law. *J. Theor. Biol.* **225** 477-487.

[39] Cangiani A and Natalini R 2010 A spatial model of cellular molecular trafficking including active transport along microtubules. *J. Theor. Biol.* **267** 614-25.

[40] Szymańska Z and Parisot M and Lachowicz M 2014 Mathematical modeling of the intracellular protein dynamics: The importance of active transport along microtubules. *J. Theor. Biol.* **363** 118-128.

[41] Dauvergne D and Edelstein-Keshet L 2015 Application of quasi-steady state methods to molecular motor transport on microtubules in fungal hyphae. *J. Theor. Biol.* **379** 47-58.

[42] Newby, Jay M and Bressloff, Paul C. 2010 Quasi-steady state reduction of molecular motor-based models of directed intermittent search *Bulletin of mathematical biology* **72** 1840-1866.

[43] Kalinay P and Percus J K 2005 Projection of two-dimensional diffusion in a narrow channel onto the longitudinal dimension. *J. Chem. Phys.* **122** 204701.

[44] Dagdug L and Pineda I 2012 Projection of two-dimensional diffusion in a curved midline and narrow varying width channel onto the longitudinal dimension. *J. Chem. Phys.* **137** 024107.

[45] Reguera D, Schmid G, Burada P, Rubí J, Reimann P and Hänggi P 2006 Entropic Transport: Kinetics, Scaling, and Control Mechanisms.*Phys. Rev. Lett.* **96** 130603.

[46] Novak I L, Kraikivski P and Slepchenko B M 2009 Diffusion in cytoplasm: effects of excluded volume due to internal membranes and cytoskeletal structures. *Biophys. J.* **97** 758-767.

[47] Ramirez J M, Thomann E A and Waymire E C 2013 Advection-Dispersion Across Intefaces. *Stat. Sci.* **28** 487-509.

[48] Ovaskainen O and Cornell S J 2003 Biased movement at a boundary and conditional occupancy times for diffusion processes. *J. Appl. Prob.* **40** 557-580.

[49] Appuhamillage T, Bokil V, Thomann E, Waymire E and Wood B 2011 Occupation and local times for skew Brownian motion with applications to dispersion across an interface. *Ann. Appl. Probab.* **21** 183-214.

[50] Doering C R, Mao X and Sander L M 2018 Random walker models for durotaxis. *Phys. Biol.* **15** 066009.

[51] Lejay A and Pichot G 2012 Simulating diffusion processes in discontinuous media: A numerical scheme with constant time steps. *J. Comput. Phys.* **231** 7299-7314.

[52] Ramirez J M 2011 Multi-skewed Brownian motion and diffusion in layered media. *Proc. Am. Math. Soc.* **139** 3739-3739.

[53] Ramirez J M, Thomann E A, Waymire E C, Haggerty R and Wood B 2006 A Generalized Taylor-Aris Formula and Skew Diffusion. *Multiscale Model. Simul.* **5** 786-801.

[54] Lejay A and Maire S 2013 New Monte Carlo schemes for simulating diffusions in discontinuous media. *J. Comput. Appl. Math.* **245** 97-116.

[55] Bielska E, Schuster M, Roger Y, Berepiki A, Soanes D M, Talbot N J and Steinberg G 2014 Hook is an adapter that coordinates kinesin-3 and dynein cargo attachment on early endosomes. *J. Cell Biol.* **204** 989-1007.

[56] Guimaraes S C, Schuster M, Bielska E, Dagdas G, Kilaru S, Meadows B R A, Schrader M and Steinberg G 2015 Peroxisomes, lipid droplets, and endoplasmic reticulum "hitchhike" on motile early endosomes. *J. Cell Biol.* **211** 945-954.

[57] Lai X, Brown, A and Xue, C 2018 A stochastic model that explains axonal organelle pileups induced by a reduction of molecular motors. *J. R. Soc. Interface* **15** 20180430.

[58] Steinberg G, Perez-Martin J 2008 Ustilago maydis, a new fungal model system for cell biology. *Trends Cell Biol.* **18** 61-67.

[59] Kuznetsov I A and Kuznetsov A V 2015 Comparison between the diffusion-reaction and slow axonal transport models for predicting tau distribution along an axon. *Math. Med. Biol.* **32** 263-283.

[60] Kloeden P and Platen E 1992 Numerical solution of stochastic differential equations. Applications of Mathematics, Springer-Verlag, Berlin.

A Stochastic simulation of particle paths for the 3-D model

In the case where $\Omega \neq \Omega_C$ for the particle motion described in Section 2.1, there is an interface $\mathcal{C} := \{(x, y, z) : x \in [0, L], y^2 + z^2 = R_0\} \subset \partial\Omega_C$ with a discontinuous jump in diffusivity. We use stochastic simulations of particle paths with a constant time step dt in order to investigate the particle spatial distribution in steady state of the system.

To simulate the bi-directional directed transport, we assign particles to one of the three possible states $s_t \in \{-1, 0, +1\}$: $s = \pm 1$ correspond to directed transport along the MT orientation and its inverse orientation respectively while the state $s = 0$ corresponds to drift diffusion. The simulation of directed transport $s = \pm 1$ and the transition between different states is implemented using discrete time and continuous space and generating evenly distributed random variables with the following transition rates

	$x_t \in \Omega_C$		
s_t	-1	0	1
-1	0	w_d	ω
0	$w_a/2$	0	$w_a/2$
1	ω	w_d	0

To implement the diffusion process in our 3-D model, we amend the direct simulation scheme for 1-D skew diffusion with a constant time step dt as introduced in [51, 54]. The direct scheme first calculates the probability to arrive at each of the two sides of the interface, makes a decision on which side to move for the next position, and then simulates its next position in that chosen region. This 1-D simulation method has been extended to a 2-D diffusion process with a hyper plane interface [54]. In our 3-D model, the interface at cross section is a circle; for a curved interface in 2-D domain, we consider small enough time step such the expected motion of the particle is small compared to the local radius of the interface. Explicitly, the simulation procedure is as detailed below.

(a1) For a given time step dt, we set up an interface layer $\mathcal{I}_{dt} := \{(x, r) \in \Omega | r \in [R_0 - c\sqrt{2D^-_{\text{lat}}dt}, R_0 + c\sqrt{2D^+_{\text{lat}}dt}], x \in [0, L]\}$. Thus a particle outside this interface layer has a probability $\alpha_c = 2\Phi(-c)$ reaching the interface within time dt where Φ is the cumulative distribution function of the standard normal distribution. In particular, we use $c = 5$, which gives the probability $\alpha_c = 5.7 \times 10^{-7}$. We also set smaller time step δt such that the boundary of the new interface layer $\mathcal{I}_{\delta t}$ with the time step δt has a distance less than dR_0 to the interface $\mathcal{C}$. Here we choose $d = 0.02$. We update positions according to below:

(b1) If a particle is outside the interface layer, then we simulate its next position after time dt by using a Euler scheme [60] for the drift diffusion.

(b2) If a particle is inside the interface layer, then we approximate its local curved boundary by its tangent plane perpendicular to the vector from the center of the cross section to the current position, then update its position for $dt/\delta t$ steps as follows. At each timestep δt, if a particle is outside the new interface layer $\mathcal{I}_{\delta t}$, then we simulate its next position using the Euler scheme for drift diffusion with a time step δt; otherwise, we do the following:

(c1) we move it along the lateral direction towards the center in the cross section using the direct scheme for skew diffusion introduced in [51];

(c2) we simulate its first hitting time τ to the interface $\mathcal{C}$ in the lateral direction using an inverse Gaussian distribution [51] and move it along the tangent direction in the cross section in two steps if $\tau < \delta t$ (otherwise we use the corresponding drift and diffusion rate to update its position): firstly, we simulate the path for a time step τ along the tangent plane in the cross section using the corresponding lateral diffusion rate; secondly, we simulate the path for the remaining time step $\delta t - \tau$ along the tangent plane using the mixing scheme method [54] with mixed lateral diffusion rate $D^-_{\text{lat}}\alpha + D^+_{\text{lat}}(1-\alpha)$ where $\alpha := \frac{\sqrt{D^-_{\text{lat}}}}{\sqrt{D^-_{\text{lat}}}+\sqrt{D^+_{\text{lat}}}}$ is the parameter for the corresponding skew Brownian motion, concerning the proportion of mean occupation time in one region.

(c3) we apply a similar two-steps simulation (one time step τ and the other $\delta t - \tau$) as in step (c2) for the axial diffusion and the drift simultaneously. This two-step approximation for the drift diffusion along the x-axis takes advantage of the fact that the interface does not depend on x.

Considering the model assumptions for the boundary, we specify:

- a reflecting boundary condition on the boundary $\partial\Omega$ for diffusion process.
- particles in directed transport state immediately reverse direction when reaching $x = 0$ or L.

Our simulation results use a time step $dt = 0.01\ s$ and the spatial distribution is obtained from a time average over 2×10^{10} steps. With no drift and no binding, i.e. $v = w_a = 0$, the simulation (not shown) gives an even distribution as expected from the model even with discontinuity in the diffusion rate.

B Dimensionless analysis of the 3-D model

We can transform the 3-D model (5) into a dimensionless form. By setting $\tau = \omega t$, $s = r/R$ and $\xi = x/L$, and also setting $s_0 = R_0/R \in [0,1]$ which is the radius ratio of inner and outer cylinders, the equations in (5) can be written as

$$\begin{aligned}
0 = &\ \tfrac{D^-_{\rm ax}}{\omega L^2}\rho_{\xi\xi} + \tfrac{1}{sR^2}\tfrac{\partial}{\partial s}(s\tfrac{D^-_{\rm lat}}{\omega}\rho_s) - \tfrac{v}{\omega L}\rho_\xi, && s\in[s_0,1],\ \xi\in[0,1]\\
0 = &\ \tfrac{D^+_{\rm ax}}{\omega L^2}\rho_{\xi\xi} + \tfrac{1}{sR^2}\tfrac{\partial}{\partial s}(s\tfrac{D^+_{\rm lat}}{\omega}\rho_s) - \tfrac{v}{\omega L}\rho_\xi - (\tfrac{w_a}{\omega}\rho - \tfrac{w_d}{\omega}\rho^+ - \tfrac{w_d}{\omega}\rho^-), && s\in[0,s_0],\ \xi\in[0,1]\\
0 = &\ \mp\tfrac{u}{\omega L}\tfrac{\partial\rho^\pm}{\partial\xi} + \tfrac{w_a}{2\omega}\rho - \tfrac{w_d}{\omega}\rho^\pm + (\rho^\pm - \rho^\mp), && s\in[0,s_0],\ \xi\in[0,1]
\end{aligned} \tag{B.1}$$

subject to boundary conditions:

$$\begin{aligned}
&J_{\rm ax} := \tfrac{D_{\rm ax}(s)}{L}\rho_\xi - v\rho = 0, && s\in[0,1],\ \xi = 0,1\\
&J_{\rm lat} := \tfrac{D_{\rm lat}}{R}\rho_s = 0, && s = 1,\ \xi\in[0,1]\\
&J_{\rm ax}, J_{\rm lat}, \rho \text{ continuous }, && s = s_0,\ \xi\in[0,1]\\
&\rho^+ = \rho^-, && s\in[0,s_0],\ \xi = 0,1
\end{aligned}$$

If we define dimensionless parameters

$$\hat{D}^\pm_{ax} := \frac{D^\pm_{ax}}{\omega L^2},\ \hat{D}^\pm_{lat} := \frac{D^\pm_{lat}}{\omega R^2},\ \hat{v} := \frac{v}{\omega L},\ \hat{u} := \frac{u}{\omega L},\ \hat{w}_{a,d} := \frac{w_{a,d}}{\omega}$$

then Eq. (B.1) becomes:

$$\begin{aligned}
0 = &\ \hat{D}^+_{\rm ax}\rho_{\xi\xi} + \tfrac{1}{s}\tfrac{\partial}{\partial s}(s\hat{D}^+_{\rm lat}\rho_s) - \hat{v}\rho_\xi, && s\in[s_0,1],\ \xi\in[0,1]\\
0 = &\ \hat{D}^-_{\rm ax}\rho_{\xi\xi} + \tfrac{1}{s}\tfrac{\partial}{\partial s}(s\hat{D}^-_{\rm lat}\rho_s) - \hat{v}\rho_\xi - (\hat{w}_a\rho - \hat{w}_d\rho^+ - \hat{w}_d\rho^-), && s\in[0,s_0],\ \xi\in[0,1]\\
0 = &\ \mp\hat{u}\tfrac{\partial\rho^\pm}{\partial\xi} + \tfrac{\hat{w}_a}{2}\rho - \hat{w}_d\rho^\pm + (\rho^\pm - \rho^\mp), && s\in[0,s_0],\ \xi\in[0,1].
\end{aligned} \tag{B.2}$$

with boundary conditions:

$$\begin{aligned}
&\hat{J}_{\rm ax} := \hat{D}_{\rm ax}(s)\rho_\xi - \hat{v}\rho = 0, && s\in[0,1],\ \xi = 0,\ 1\\
&\hat{J}_{\rm lat} := \hat{D}_{\rm lat}\rho_s = 0, && s = 1,\ \xi\in[0,1]\\
&\hat{J}_{\rm ax}, \hat{J}_{\rm lat}, \rho \text{ continuous }, && s = s_0,\ \xi\in[0,1]\\
&\rho^+ = \rho^-, && s\in[0,s_0], \xi = 0,1.
\end{aligned}$$

Reorganizing Eq. (B.2) gives

$$\begin{aligned}
0 = &\ \rho_{\xi\xi} + \tfrac{Q^+}{s}\tfrac{\partial}{\partial s}(s\rho_s) - Pe^+\rho_\xi, && s\in[s_0,1],\ \xi\in[0,1]\\
0 = &\ \rho_{\xi\xi} + \tfrac{Q^-}{s}\tfrac{\partial}{\partial s}(s\rho_s) - Pe^-\rho_\xi - (W_a\rho - W_d\rho^+ - W_d\rho^-), && s\in[0,s_0],\ \xi\in[0,1]\\
0 = &\ \mp U\tfrac{\partial\rho^\pm}{\partial\xi} + \tfrac{W_a}{2}\rho - W_d\rho^\pm + \tfrac{1}{\hat{D}^-_{ax}}(\rho^\pm - \rho^\mp), && s\in[0,s_0],\ \xi\in[0,1]
\end{aligned} \tag{B.3}$$

where $Pe^\pm := \frac{\hat{v}}{\hat{D}^\pm_{ax}} = \frac{vL}{D^\pm_{ax}}$, $Q^\pm := \frac{L^2 D^\pm_{lat}}{R^2 D^\pm_{ax}}$, $W_{a,d} := \frac{\hat{w}_{a,d}}{\hat{D}^-_{ax}} = \frac{w_{a,d}L^2}{D^-_{ax}}$ and $U := \frac{\hat{u}}{\hat{D}^-_{ax}} = \frac{uL}{D^-_{ax}}$.

C QSS reduction for the 1-D model

Here we discuss QSS reduction to support the reduced 1-D scalar equation of the total density profile in the main text. The procedure follows from [41, 42]. The first step of the QSS reduction involves rescaling x and t so that the cell length is $L = 1$ and a typical particle moving speed is 1. Now the rescaled matrix equation is of the form

$$\frac{\partial \mathbf{p}}{\partial t} = \frac{1}{\epsilon} A\mathbf{p} + M(\mathbf{p}) \tag{C.1}$$

We decompose an arbitrary state vector $\mathbf{p}$ into its uniform steady state value $\mathbf{P^{ss}} := \frac{w_d}{w_a+w_d}(\frac{w_a}{2w_d}, \frac{w_a}{2w_d}, 1)^T$ plus a (spatially nonuniform) deviation $\mathbf{w}$,

$$\mathbf{p} = P\mathbf{P^{ss}} + \mathbf{w}. \tag{C.2}$$

$\mathbf{P^{ss}}$ is the normalized eigenvector of the transition matrix A such that $\Psi^T \mathbf{P^{ss}} = 1$ (here the vector $\Psi = (1, 1, 1)^T$) for eigenvalue 0, and the overall particle density is $P = \Psi^T \mathbf{p}$. Multiplying Ψ^T in Eq. (C.2) we have $\Psi^T \mathbf{w} = 0$. Note that $\Psi^T A = 0$. Multiplying Eq. (C.1) with Ψ^T we have

$$\frac{\partial P}{\partial t} = \Psi^T M(P\mathbf{P^{ss}} + \mathbf{w}). \tag{C.3}$$

Note $\mathbf{w} = \mathbf{p} - P\mathbf{P^{ss}}$ and $A\mathbf{P^{ss}} = 0$ as $\mathbf{P^{ss}}$ is the eigenvector for eigenvalue 0, then

$$\frac{\partial \mathbf{w}}{\partial t} = \frac{\partial \mathbf{p}}{\partial t} - \frac{\partial P}{\partial t}\mathbf{P^{ss}} = \frac{1}{\epsilon} A(P\mathbf{P^{ss}} + \mathbf{w}) + M(P\mathbf{P^{ss}} + \mathbf{w}) - \mathbf{P^{ss}}\Psi^T M(P\mathbf{P^{ss}} + \mathbf{w}) \tag{C.4}$$

$$= \frac{1}{\epsilon} A\mathbf{w} + (I - \mathbf{P^{ss}}\Psi^T)M(P\mathbf{P^{ss}} + \mathbf{w}) \tag{C.5}$$

We make an asymptotic expansion $\mathbf{w} = \mathbf{w_0} + \epsilon \mathbf{w}_1 + \cdots$. To the leading order we have $A\mathbf{w}_0 = 0$. As A has one zero eigenvalue and $\Psi^T \mathbf{w}_0 = 0$, we have $\mathbf{w}_0 = \mathbf{0}$. The $O(1)$ terms result in the following relation for $\mathbf{w}_1$:

$$A\mathbf{w}_1 = (\mathbf{P^{ss}}\Psi^T - I)M(P\mathbf{P^{ss}}) \tag{C.6}$$

We decompose $\mathbf{w}_1$ into terms of the form:

$$\mathbf{w}_1 = -\theta P_x + \mathbf{q} P_{xx} \tag{C.7}$$

where θ and $\mathbf{q}$ are undetermined vectors. Expanding Eq. (C.6) we have

$$A(-\theta P_x + \mathbf{q}P_{xx}) = \mathbf{P^{ss}}(-\langle v\rangle P_x + \langle D\rangle P_{xx}) - \begin{pmatrix} -v_1 P_1^{ss} P_x + D_1 P_1^{ss} P_{xx} \\ -v_2 P_2^{ss} P_x + D_2 P_2^{ss} P_{xx} \\ -v_3 P_3^{ss} P_x + D_3 P_3^{ss} P_{xx} \end{pmatrix} \tag{C.8}$$

where $\langle\cdot\rangle$ is the weighted mean using entries of the vector $\mathbf{P}^{ss}$ as the weights. Explicitly $\langle v\rangle = \frac{v}{u}\frac{w_d}{w_a+w_d}$ and $\langle D\rangle = \frac{w_d D_{ax}}{uL(w_a+w_d)}$. Then

$$A\theta = -\begin{pmatrix} (v_1-\langle v\rangle)P_1^{ss} \\ (v_2-\langle v\rangle)P_2^{ss} \\ (v_3-\langle v\rangle)P_3^{ss} \end{pmatrix} \text{ and } A\mathbf{q} = \begin{pmatrix} (D_1-\langle D\rangle)P_1^{ss} \\ (D_2-\langle D\rangle)P_2^{ss} \\ (D_3-\langle D\rangle)P_3^{ss} \end{pmatrix}. \tag{C.9}$$

The vector θ can be determined through $\Psi^T\mathbf{w}_1 = 0$ which gives

$$\begin{aligned} \theta_1 &= -(\tfrac{\langle v\rangle}{w_a+w_d} - \tfrac{1}{2\omega+w_d})\tfrac{uP_1^{ss}}{\epsilon L} \\ \theta_2 &= -(\tfrac{\langle v\rangle}{w_a+w_d} + \tfrac{1}{2\omega+w_d})\tfrac{uP_1^{ss}}{\epsilon L} \\ \theta_3 &= \tfrac{2\langle v\rangle}{w_a+w_d}\tfrac{uP_1^{ss}}{\epsilon L} \end{aligned} . \tag{C.10}$$

Substituting the expansion for $\mathbf{w}_1$ (C.7) into the scalar equation (C.3) gives

$$P_t = -\langle v\rangle P_x + \langle D\rangle P_{xx} + \epsilon\sum_{j=1}^{3}(v_j\theta_j P_{xx} - (v_j q_j + D_j\theta_j)P_{xxx} + q_j D_j P_{xxxx}) \tag{C.11}$$

Assuming diffusivities in order of $O(\epsilon)$, vector components q_j are then in order of $O(\epsilon)$. This leads to

$$\partial_t P = -V\partial_x P + D\partial_x^2 P, \quad x\in[0,1] \tag{C.12}$$

where $V = \langle v\rangle = \frac{v}{u}\frac{w_d}{w_a+w_d}$ and $D = \langle D\rangle + \epsilon\mathbf{v}^T\theta = \frac{w_d D_{ax}}{uL(w_a+w_d)} + (\frac{1}{2\omega+w_d} + \frac{v^2 w_d}{u^2(w_a+w_d)^2})\frac{uw_a}{L(w_a+w_d)}$.

Boundary conditions $\rho^+ = \rho^-$ at $x = 0,1$ and $D_3\rho_x - v_3\rho = 0$ at $x = 0,1$ satisfy $v_1\rho^+ + v_2\rho^- + v_3\rho - D_3\rho_x = 0$ at $x = 0,1$. By noting

$$\begin{aligned} \rho^+ &= PP_1^{ss} + \epsilon(-\theta_1 P_x + \cdots) \\ \rho^- &= PP_2^{ss} + \epsilon(-\theta_2 P_x + \cdots) \\ \rho &= PP_3^{ss} + \epsilon(-\theta_3 P_x + \cdots) \end{aligned}$$

this corresponds to boundary condition $VP - DP_x = 0, x = 0,1$.

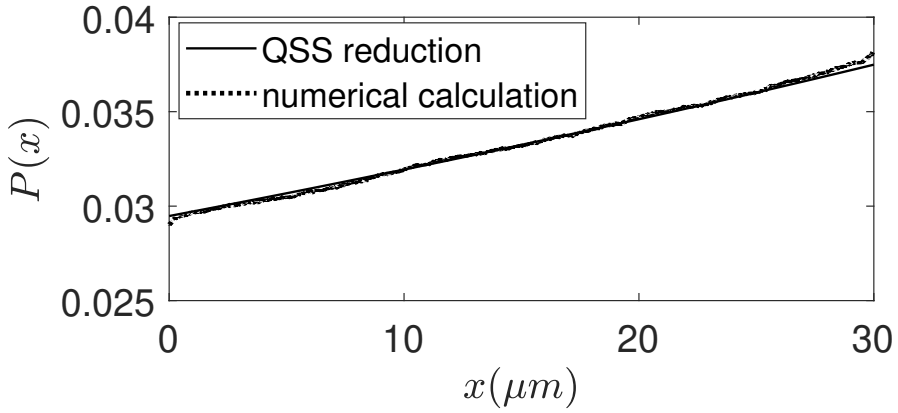

Figure C.1: An example of QSS approximation of total density from Eq. (C.12). Parameters are: $w_a = 1/s$, $w_d = 1.7/s$, $\omega = 1.2/s$, $u = 2\mu m/s$, $v = 0.005\mu m/s$, $D = 0.05\mu m^2/s$.